



## Phase-change composite filled natural nanotubes in hydrogel promote wound healing under photothermally triggered drug release

Jing-Jing Ye<sup>a</sup>, Long-Fei Li<sup>a</sup>, Rui-Nan Hao<sup>a</sup>, Min Gong<sup>a</sup>, Tong Wang<sup>a</sup>, Jian Song<sup>a</sup>,  
Qing-Han Meng<sup>b</sup>, Na-Na Zhao<sup>c</sup>, Fu-Jian Xu<sup>c</sup>, Yuri Lvov<sup>d,\*\*\*</sup>, Li-Qun Zhang<sup>a,\*\*</sup>, Jia-Jia Xue<sup>a,\*</sup>

<sup>a</sup> Beijing Laboratory of Biomedical Materials, State Key Laboratory of Organic-Inorganic Composites, Beijing University of Chemical Technology, Beijing, 100029, PR China

<sup>b</sup> College of Materials Science and Engineering, Beijing University of Chemical Technology, Beijing, 100029, PR China

<sup>c</sup> Beijing Laboratory of Biomedical Materials, Beijing University of Chemical Technology, Beijing, 100029, PR China

<sup>d</sup> Institute for Micromanufacturing and Biomedical Engineering Program, Louisiana Tech University, Ruston, LA, 71272, USA

### ARTICLE INFO

#### Keywords:

Anti-bacteria  
Clay nanotubes  
Alginate hydrogel  
Phase-change material  
NIR-Triggered drug release  
Infected wound healing

### ABSTRACT

It is of great importance to treat a bacterial-infected wound by a smart dressing capable of delivering antibiotics in a smart manner without causing drug resistance. The construction of smart release nanocontainers responsive to near-infrared (NIR) laser irradiation in an on-demand and stepwise way is a promising strategy for avoiding the emergence of multidrug-resistant bacteria. Here, we develop a hydrogel composite made of alginate and nanotubes with an efficient NIR-triggered release of rifampicin and outstanding antibacterial ability. This composite hydrogel is prepared through co-encapsulating antibacterial drug (rifampicin), NIR-absorbing dye (indocyanine green), and phase-change materials (a eutectic mixture of fatty acids) into halloysite nanotubes, followed by incorporation into alginate hydrogels, allowing the in-situ gelation at room temperature and maintaining the integrity of drug-loaded nanotubes. Among them, the eutectic mixture with a melting point of 39 °C serves as the biocompatible phase-change material to facilitate the NIR-triggered drug release. The resultant phase-change gated-nanotubes exhibit a prominent photothermal efficiency with multistep drug release under laser irradiation. In an *in vitro* assay, composite hydrogel provides good antibacterial potency against *Staphylococcus aureus*, one of the most prevalent microorganisms of dangerous gas gangrene. A bacterial-infected rat full-thickness wound model demonstrates that the NIR-responsive composite hydrogel inhibits the bacteria colonization and suppresses the inflammatory response caused by bacteria, promoting angiogenesis and collagen deposition to accelerate wound regeneration. The NIR-responsive composite hydrogel has a great potential as an antibacterial wound dressing functionalized with controlled multistep treatment of the infected sites.

### 1. Introduction

Bacterial infection during wound healing and skin regeneration is a serious threat to public health [1,2]. Although antibiotics are the main weapon of the war against bacteria, the clinical abuse of antibiotics has accelerated the appearance of multidrug-resistant bacteria and the formation of biofilms [3–5]. Therefore, it is urgent to explore smart and effective antibacterial strategies for making revised use of antibiotics, at

which concertation at the site is decreased with time after application that may allow for new bacterial proliferation. One of the most promising options is a smart wound dressing capable of delivering the payload to the site in a controllable and sustained manner [6–8].

Near-infrared (NIR) laser irradiation, with advantages of deep tissue penetration, non-invasiveness, and spatiotemporal controllability, has been applied for treating bacterial infection. Matrix materials, such as hydrogel and electrospun nanofiber scaffolds, have been incorporated

Peer review under responsibility of KeAi Communications Co., Ltd.

\* Corresponding author.

\*\* Corresponding author.

\*\*\* Corresponding author.

E-mail addresses: [ylvov@latech.edu](mailto:ylvov@latech.edu) (Y. Lvov), [zhanglq@mail.buct.edu.cn](mailto:zhanglq@mail.buct.edu.cn) (L.-Q. Zhang), [jjjiaxue@mail.buct.edu.cn](mailto:jjjiaxue@mail.buct.edu.cn) (J.-J. Xue).

<https://doi.org/10.1016/j.bioactmat.2022.08.026>

Received 2 May 2022; Received in revised form 23 August 2022; Accepted 23 August 2022

2452-199X/© 2022 The Authors. Publishing services by Elsevier B.V. on behalf of KeAi Communications Co. Ltd. This is an open access article under the CC BY-NC-ND license (<http://creativecommons.org/licenses/by-nc-nd/4.0/>).

with photothermal agents to serve as NIR-responsive antibacterial wound dressings [9]. The photothermal agents convert light to thermal energy, causing a local hyperthermia to denaturalize bacterial proteins and killing bacteria. Various types of photothermal agents have been incorporated to wound dressings, such as antimonene nanosheets [10], gold nanorods [11], graphene [12], cuttlefish melanin nanoparticles [13], and catechol- $\text{Fe}^3$  [14]. However, in most cases of applying NIR for the treatment of bacterial infection, it is often necessary to maintain at a high temperature for a certain period of time for the complete denaturation of bacterial proteins [15,16], which may also cause damage to the surrounding tissues.

NIR irradiation can also be applied as an external stimulation to trigger controlled drug release, promoting the healing of bacterial infected wound [15,17]. Various types of nanoparticles [18], nanofibers [19], microspheres [20], and nanotubes [21] have been developed as the drug carriers for triggered release. For example, a NIR-triggered system based on hollow microspheres allowed for the controlled release of antibiotics *via* a “molecular switch” [22]. In another study, drugs were adsorbed on the surface of polydopamine nanoparticles *via*  $\pi$ - $\pi$  stacking and hydrogen bonding, and the drug was released upon laser irradiation [23]. Due to the complicated requirements on the support structures and functional groups of the drugs, currently available formulations for NIR-triggered drug delivery system are still very limited.

Natural halloysite clay nanotubes (HNTs) have been employed as the reservoir for encapsulating antibiotics because of their hollow structure, low price, and good biocompatibility [24,25]. On-demand sustained drug release is expected when the nanotubes are co-loaded with heat-sensitive gatekeepers, like NIR-responsive materials that periodically open with laser pulsing transportation from halloysite lumens. Phase-change materials (PCMs) are promising and popular gatekeepers

because they can undergo a reversible solid-liquid transition under heating [3,18,26–29]. Fatty acids are preferable candidates owing to their low cost, biocompatibility, and biodegradability [30]. A eutectic mixture of lauric acid and stearic acid at a weight ratio of 4:1 exhibits a sharp melting point at 39 °C, which may serve as the gating material for heat-triggered drug delivery [18].

Hydrogels have been widely used in wound healing and tissue regeneration due to their similarity with the extracellular matrix micro-environment [16,31]. Alginate, a Food and Drug Administration approved polysaccharide [32], plays an important role in wound healing [33,34] and tissue engineering [35–37]. Alginate macromolecules can be gelled using calcium ions as the cross-linking agent [35,38,39], and the resultant material has high water content, elasticity, permeability, and capability to contain a moist environment [40]. Alginate-based hydrogels can be prepared at mild conditions [41], which is suitable as carriers for the bioactive molecules, living cells, nanoscale containers-loaded with bioactive compounds and PCMs. When being directly loaded in the alginate hydrogel, the drugs can be easily released by diffusion, leading to an un-controllable and excessive release, which may cause the occurrence of bacterial drug resistance. Therefore, the construction of controlled drug release system to deliver antibiotics in an on-demand and multistep way to prevent drug resistance is of high need.

We developed an NIR-responsive hydrogel drug delivery platform by integrating PCM-gated clay nanotubes to control the release of antibiotics for promoting bacterial-infected skin wound healing (Fig. 1). We firstly constructed an NIR-responsive rifampicin release platform by its co-encapsulating with indocyanine green (ICG) and fatty acids into the nanotubes. When irradiated by the NIR laser, photothermal agent ICG could convert light into local heating, leading to the temperature rise above the melting point of the fatty acids, enabling the release of

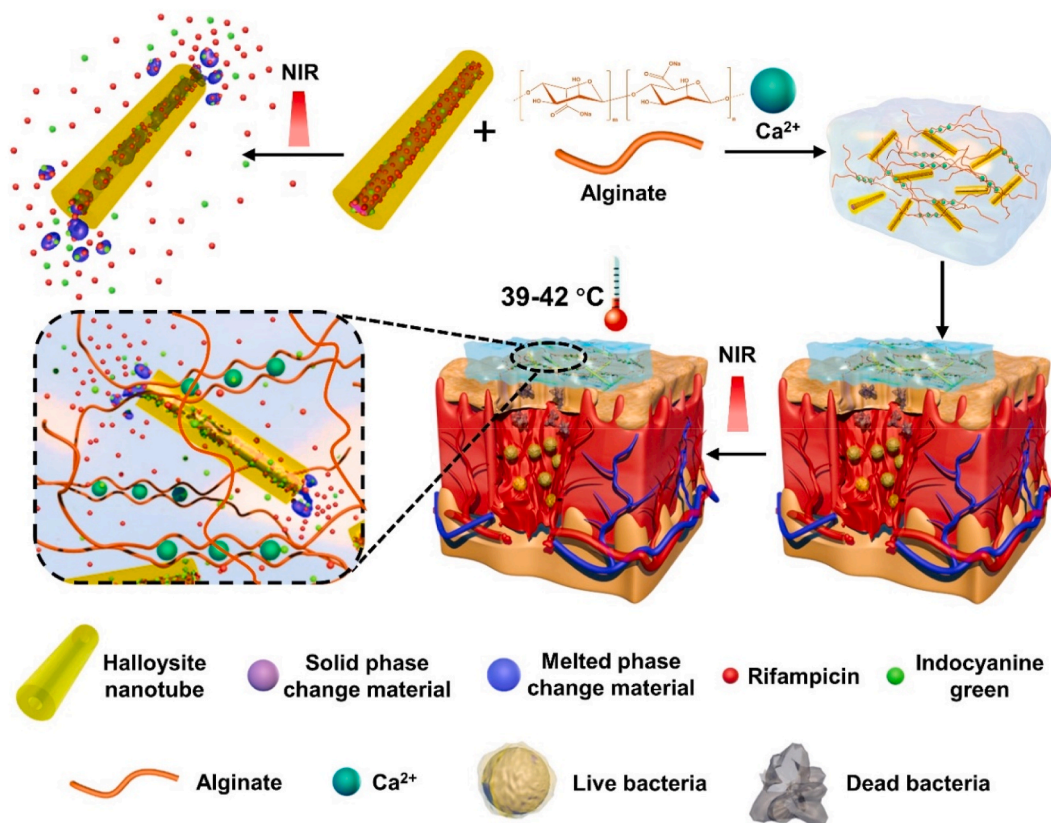


**Fig. 1.** Scheme of the NIR-triggered release of drug molecules from PCM-gated nanotubes that were integrated in alginate hydrogel to promote infected wound healing under photothermal irradiation. PCM was based on the mixture of fatty acids, while rifampicin and indocyanine green served as the antibiotic and NIR-absorbing dye.

rifampicin from the nanotubes. At the same time, the temperature was controlled below 42 °C, preventing any heat damage to the surrounding tissues and realizing the mild heat triggered bacterial killing. The obtained drug loaded HNTs was then integrated in alginate at 25 wt.% and cross-linked by divalent cations ( $\text{Ca}^{2+}$ ), allowing the in-situ gelation at room temperature. We evaluated the stepwise drug delivery profile upon sequential laser pulses. The *in vivo* anti-bacterial performance and promotion on the infected wound healing of the composite hydrogel were evaluated using a bacterial-infected rat full-thickness wound model.

## 2. Materials and methods

### 2.1. Materials

HNTs were donated by Applied Minerals Inc. (USA).  $\gamma$ -Aminopropyl triethoxysilane (APTES) was purchased from Alfa Aesar (USA). Rifampicin (98%) was purchased from TCI (Japan). Indocyanine green (ICG, 95%) was purchased from Energy Chemical (China). Dimethyl sulfoxide (DMSO) was purchased from Aladdin (China). Lauric acid (97%) and stearic acid (95%) were purchased from Sigma-Aldrich (USA). Sodium alginate (low viscosity) was purchased from J&K (China).  $\text{CaCl}_2$  (AR, 96.0%) was purchased from Aladdin (China). Cell counting kit-8 (CCK-8) was purchased from WISSEN. Dulbecco's modified eagle medium (DMEM) was purchased from Gibco (USA). 4',6-Diamidino-2-phenylindole (DAPI) was purchased from Solarbio (China). Alexa Fluor 568-phalloidin and LIVE/DEAD BacLight bacterial viability kit were purchased from Invitrogen (USA). *Staphylococcus aureus* (*S. aureus*) was purchased from ATCC (China). Anti-IL-6 antibody (bs-0782R) was purchased from Bioss (China). Anti-CD31 antibody (ab182981), anti-TNF- $\alpha$  antibody (ab212899), and anti-collagen III antibody (ab6310) were purchased from Abcam (U.K). Anti-collagen I antibody (PA1-26204) was purchased from Invitrogen. All the secondary antibodies were purchased from Servicobio (China).

### 2.2. Modification of halloysite nanotubes

APTES was firstly employed to modify the surface of HNTs for better dispersion in DMSO according to the previous report [25]. Briefly, 500  $\mu\text{L}$  of APTES was dissolved in 6.25 mL of toluene, and the suspension was sonicated for 30 min after 0.15 g of HNTs was added, followed by refluxing at 120 °C for 8 h under continuous stirring. The resultant mixture was then centrifuged at 5000 rpm for 5 min, and the sediment was dried overnight at 120 °C after washing with fresh toluene 6 times to remove the unreacted APTES. The obtained nanotubes were labeled as HNT-KH550. Thermogravimetric analysis (TGA, Mettler-Toledo International Inc., Switzerland) was utilized to determine the degree of APTES grafting according to the previous report [25].

### 2.3. Loading of rifampicin into the modified nanotubes

The nanotubes loaded with PCM and ICG, without drug, were prepared by vacuum, and the obtained sample was labeled as HPI. To explore the appropriate ratio of ICG and PCM, nanotubes loaded with ICG and PCM at different ratios of 0.1, 0.05, 0.01, 0.005, and 0.001 were prepared, and the obtained nanotubes were labeled as HPI-0.1, HPI-0.05, HPI-0.01, HPI-0.005, and HPI-0.001, respectively. Rifampicin was further mixed with the PCM and ICG and then loaded in the hollow cavities of the nanotubes. In a typical process, 240 mg of HNT-KH550, 1200 mg of lauric acid, 300 mg of stearic acid, 600 mg of rifampicin, and 7.5 mg of ICG were dissolved in 6 mL of DMSO under stirring. After sonicated and dispersed for 30 min at 25–30 °C, the suspension was transferred to a vacuum jar and evacuated for 15 min, followed by connection to the atmospheric pressure for another 5 min. The loading process was repeated 3 times to enhance the loading efficiency. The drug-loaded nanotubes were obtained through centrifuging at 5000 rpm

for 5 min and washing with DMSO for twice to remove the excess cargos. Then, 6 mL of deionized (DI) water was added to the above precipitate, leading to the fatty acids solidification and the rifampicin and ICG retaining inside the nanotubes. The obtained precipitate was then washed several times with DI water and centrifuged at 4000 rpm for 3 min at 10 °C, a temperature below the melting point of PCM, which could prevent PCM from melting. The obtained drug-loaded nanotubes were labeled as HPR.

### 2.4. Photothermally triggered release of antibacterial drug from the nanotubes

Firstly, 1 mL of HPI-0.1, HPI-0.05, HPI-0.01, HPI-0.005, and HPI-0.001 suspensions (4 mg/mL) were added into the wells of a 24-well plate, respectively. Subsequently, the suspension was irradiated by an 808 nm NIR laser (Changchun Optoelectronics, LR-MFJ-808/5000 mW) at 3.0 W/cm<sup>2</sup> for 6 min. The temperature changes and the corresponding thermal images were recorded by an infrared camera (FLIR E75). The temperature change of DI water was also recorded as a control.

The loading content of the drug in the nanotubes was measured. Briefly, 20 mg of HPR was dispersed in 5 mL of ethanol and sonicated for 30 min, and then the solution was centrifuged at 4000 rpm for 5 min. Afterwards, 5 mL supernatant was retrieved, and the precipitates were re-suspended with 5 mL of fresh ethanol. The amount of rifampicin released in the supernatant was analyzed by a microplate reader at 480 nm. This process was repeated for several times until no rifampicin could be tested in the supernatant.

The cumulative release profiles of rifampicin from the HPR suspension (100 mg/mL) upon laser irradiation were measured. Briefly, 20 mg of HPR was dispersed in 200  $\mu\text{L}$  of DI water, and then the mixture was irradiated by a NIR laser at 3.0 W/cm<sup>2</sup> for 6 min. At indicated time points, the solution was centrifuged at 4000 rpm for 3 min at 10 °C. Then, the supernatant was retrieved, and the precipitates were re-suspended with 200  $\mu\text{L}$  of DI water. The amount of rifampicin released in the supernatant was analyzed by a microplate reader (Epoch) at 480 nm. The mixture was left in the absence of light at room temperature for another 6 min, and the rifampicin in the solution was tested by the same way. This irradiation procedure was repeated for several rounds, and the photothermal stability and cycling performance of the HPR was tested by recording the temperature values and the corresponding thermal images by FLIR E75. The cumulative release profile of rifampicin from the HPR suspension without NIR laser irradiation was investigated as a control. The HPR suspensions (100 mg/mL) irradiated by the NIR laser for 12 and 15 rounds were labeled as HPR<sub>12</sub> and HPR<sub>15</sub>, respectively. Furthermore, the internal structure of HNT-KH550, HPR, HPR<sub>12</sub>, and HPR<sub>15</sub> were analyzed with transmission electron microscopy (TEM, JEM-2100F) at 120 kV.

We also encapsulated rhodamine B, a fluorescence dye, in the nanotubes along with PCM to better visualize the release of the encapsulated payloads. For visualizing the release process, 4 mg rhodamine B-loaded nanotubes was suspended in 200  $\mu\text{L}$  DI water and then added into the well of a 24-well plate, and then hot water (>60 °C) was added to the suspension and remained stable. The area covered by rhodamine B in the suspension was observed under a fluorescent inverted microscope (Axio Observer 3) with the change in time after the addition of hot water.

### 2.5. Preparation of composite hydrogels

Firstly, a homogeneous alginate sodium solution was prepared by dissolving 2 g of alginate sodium in 100 mL of sterile DI water by stirring, and 0.5 g of  $\text{CaCl}_2$  was dissolved in 100 mL of sterile DI water under stirring to prepare a homogeneous  $\text{CaCl}_2$  solution. To determine the optimal amount of HPR in the alginate matrix, different amounts of HPR (ca., 0, 5, 10, 20, 25, 30 wt.%) were added. Briefly, 0, 8, 16, 32, 40, and 48 mg of HPR were dispersed in 8 mL alginate sodium solution, respectively, and then cross-linked by 8 mL of  $\text{CaCl}_2$  solution to obtain

the composite hydrogels. Then, the hydrogels were cut into cylinders (diameter: 15 mm, thickness: 1 mm) and washed with DI water for several times to remove the excess alginate sodium and  $\text{CaCl}_2$ . The obtained hydrogels were labeled as ALG-HPR-0, ALG-HPR-5, ALG-HPR-10, ALG-HPR-20, ALG-HPR-25, and ALG-HPR-30, respectively. As control groups, pristine alginate hydrogel (ALG) and alginate hydrogel containing HP (ALG-HP) were also fabricated using the same protocol.

## 2.6. Photothermal behaviors of the composite hydrogels

The photothermal behaviors of the composite hydrogels were investigated. Briefly, the sample was immersed in 0.4 mL DI water and irradiated by the laser for 6 min at a power density of  $3.0 \text{ W/cm}^2$ , during which the volume of the DI water was mimicking the semi-dry and semi-wet wound environment. The temperature values and the corresponding thermal images were recorded. In order to elucidate the photothermal behavior of ALG-HPR hydrogel containing 25 wt.% HRP, they were placed in the well of a 24-well plate containing 0.4 mL DI water and then exposed to NIR laser. The laser was removed when the temperature of the hydrogel was increased from  $37$  to  $42$  °C, and the power density of NIR laser was set to  $1.5 \text{ W/cm}^2$  for the first 10 cycles and  $2.0 \text{ W/cm}^2$  for the last 13 cycles, respectively. Meanwhile, the temperature changes and the corresponding thermal images were recorded.

## 2.7. Drug release profile of photothermal-responsive hydrogels

The drug release profile of the ALG-HPR hydrogel was then investigated according to the versatility and convenience of laser irradiation for animal experiment. Briefly, three parallel samples of ALG-HPR hydrogels were placed in the wells of a 24-well plate with 400  $\mu\text{L}$  of DI water. Then, the ALG-HPR hydrogels were irradiated by a NIR laser for 7 min. The temperature of the hydrogel was monitored and maintained between  $39$  and  $42$  °C by tuning the power density of the laser accordingly in a range of  $1.5$ – $3.0 \text{ W/cm}^2$ . Then, the irradiated hydrogels were stocked at  $37$  °C for 24 h to allow the rifampicin to diffuse from the nanotubes and the hydrogels into the surrounding environment. At indicated time points, the irradiated supernatant was removed and analyzed by a microplate reader at 480 nm. In addition, the supernatant was retrieved and replaced with 400  $\mu\text{L}$  of DI water. The mixture of ALG-HPR hydrogels were repeatedly irradiated by NIR laser until the temperature of hydrogel could not up to  $39$  °C.

The irradiation parameter of NIR laser for triggering the release of the drug to effectively inhibit *S. aureus* growth was determined. Briefly, the ALG-HPR hydrogel was placed in the well of a 24-well plate with 400  $\mu\text{L}$  of DI water. The mixture was irradiated by NIR laser at  $3.0 \text{ W/cm}^2$  for 30 s and repeated 3 times, and then the 24-well plate was removed to a  $37$  °C constant temperature incubator for 30 min. At indicated time points, the irradiated supernatant was removed and analyzed at 480 nm using a microplate reader, and the 400  $\mu\text{L}$  of supernatant was retrieved and replaced with 400  $\mu\text{L}$  of DI water. This process was repeated three rounds.

## 2.8. In vitro cytotoxicity assay

L929 cells were selected as mode normal cells. Firstly, the ALG-HPR composite hydrogels (diameter: 15 mm, thickness: 1 mm) were sterilized under UV and placed in the wells of a 24-well plate. Then, 100  $\mu\text{L}$  of L929 cell suspension ( $2 \times 10^4$  cells/mL) and 300  $\mu\text{L}$  of cell culture medium were plated onto the hydrogels and incubated for 1 day. Afterwards, the hydrogels were irradiated under the NIR laser at  $3.0 \text{ W/cm}^2$  for 30 s, repeated 3 times, and then removed to an incubator at  $37$  °C for another 1 day. Then, 100  $\mu\text{L}$  of CCK-8 solution was added and incubated for another 4 h, and then the optical density (O.D.) values of L929 cells were measured by a microplate reader at 450 nm. The cells were then stained by DAPI and Alexa Fluor 568-phalloidin and observed under a fluorescent inverted microscope. This irradiation procedure was

then repeated at day 3, 5, and 7, respectively. The O.D. values of the L929 cells were then examined 1 day after laser irradiation. The composite hydrogel that was not irradiated with NIR laser served as the control group.

## 2.9. In vitro antibacterial activity assay

We compared the sizes of the inhibition zones of different groups. Briefly, 100  $\mu\text{L}$  of  $10^8$  CFU/mL *S. aureus* suspensions were spread uniformly onto the Luria-Bertani (LB) solid medium. Subsequently, the ALG, ALG-HP, and ALG-HPR hydrogel samples were attached to the center of LB solid mediums by sterile tweezers. The LB solid medium with *S. aureus* was set as the Blank control. As for the ALG-HP (–) NIR group and ALG-HPR (+) NIR group, the hydrogels were irradiated by the NIR laser at  $3.0 \text{ W/cm}^2$  for 30 s and repeated 3 times. Then, after incubation at  $37$  °C for 24 h, the bacterial growth was directly observed on agar plates of all groups.

The antibacterial performance of ALG-HPR hydrogels was also examined through spread plate count method. Firstly, 400  $\mu\text{L}$  of *S. aureus* suspension ( $5 \times 10^7$  CFU/mL) was co-incubated with ALG-HPR hydrogel samples. Then, hydrogels were treated in the absence and presence of NIR laser irradiation at  $3.0 \text{ W/cm}^2$  for 30 s and repeated 3 times, which were labeled as ALG-HPR (–) NIR and ALG-HPR (+) NIR, respectively. Meanwhile, the *S. aureus* in the absence and presence of NIR laser irradiation were labeled as Blank (–) NIR and Blank (+) NIR, respectively. After incubating 24 h at  $37$  °C, 10  $\mu\text{L}$  of the bacterial suspension was diluted 100 times with LB, followed by evenly spreading on LB agar plates. The plates were photographed at determined time and the developed colonies were quantified using ImageJ software to calculate the surviving ratio. To visualize the antibacterial performance of the hydrogels, the bacterial suspension was further stained with SYTO9/propidium iodide dyes for groups both treated in the absence and presence of NIR laser irradiation. Subsequently, all samples were observed via a confocal laser scanning microscope (CLSM, SP8, Leica, Germany) at  $63 \times$  oil. During the incubation, at 36 and 48 h, the irradiation procedure was repeated, respectively. The area of green fluorescence for live *S. aureus* was measured using Image Pro Plus 6.0 software.

## 2.10. In vivo wound healing experiment

Sprague-Dawley rats (6-weeks-old, 180–250 g) were purchased from Beijing HFK BioScience Co., Ltd and were housed individually in cages at standard temperature for 2 days. Briefly, the dorsal skin of the rat was dehaired using an electric shaver. After anesthesia with 3% pentobarbital (45 mg/kg), a diameter of 15 mm full-thickness excision was established on the back of each rat, then a splint model was created as previously reported [42,43]. A silicon ring (adhesive side down) was placed around the wound and secured with 4-0 non-absorbable prolene sutures. The rats were randomly divided into six groups ( $n = 18$ ): Blank, *S. aureus*, ALG, ALG-HP (+) NIR, ALG-HPR, and ALG-HPR (+) NIR. The Blank group was free of *S. aureus* infection, while in the other five groups, 200  $\mu\text{L}$  of *S. aureus* suspension ( $10^8$  CFU/mL) was added on the wounds, establishing the infected wound. The skin defects were covered by ALG, ALG-HP, ALG-HPR, and ALG-HPR hydrogels in groups of ALG, ALG-HP (+) NIR, ALG-HPR, and ALG-HPR (+) NIR, while one piece of hydrogel was used for each rat. The rats in the ALG-HP (+) NIR group and ALG-HPR (+) NIR group were treated with laser irradiation of 7 min duration on day 0, 1, 3, 5, and 7 to maintain the wound temperature at  $39$ – $42$  °C. The corresponding thermal images of ALG-HP and ALG-HPR hydrogels on skin wounds under laser irradiation at  $1.5$ – $2.0 \text{ W/cm}^2$  were recorded and plotted using an FLIR E75. The effective temperature rising curves and corresponding thermal images of ALG-HP and ALG-HPR hydrogels was maintained at  $39$ – $42$  °C for 7 min. All wounds were photographed on day 0, 3, 7, 14, and 21, and the wound area was measured using ImageJ software.

During the entire experiment, the rats were treated in accordance with the guidelines for Care and Use of Laboratory Animals of Beijing HFK BioScience Co., Ltd Animal Ethics Committee (IACUC-20201225). On the 3, 7, 14, and 21st day after surgery, through injected an excess amount of 3% pentobarbital, the rats were euthanized. The entire wound with adjacent normal skin were harvested, excised, and fixed in 4% paraformaldehyde for the histological analysis. Immunohistochemistry staining of interleukin-6 (IL-6), tumor necrosis factor- $\alpha$  (TNF- $\alpha$ ), platelet endothelial cell adhesion molecule-1 (CD31), collagen I and III was performed and measured using Image Pro Plus 6.0 software, respectively. The amount of the bacteria in the wound on day 7 were quantified through separating and homogenizing the infectious tissues in normal saline to obtain the supernatant, which was further diluted 1000 times and plated on LB agar to count and analyze the grown colonies.

2.11. Statistical analysis

All results were reported as mean  $\pm$  standard deviation. The data were analyzed by one-way ANOVA followed by Tukey's test (GraphPad Prism software) where  $p < 0.05$  meant a significant difference. (\* $p < 0.05$ ; \*\* $p < 0.01$ , \*\*\* $p < 0.001$ , ns: no significance difference.)

3. Results and discussion

3.1. Preparation and photothermal behavior of the PCM-gated natural nanotubes

A eutectic mixture of lauric acid and stearic acid was used as "gatekeepers" of the clay nanotubes for NIR-triggered drug release. Before drug loading, we firstly modified the surface of HNTs by

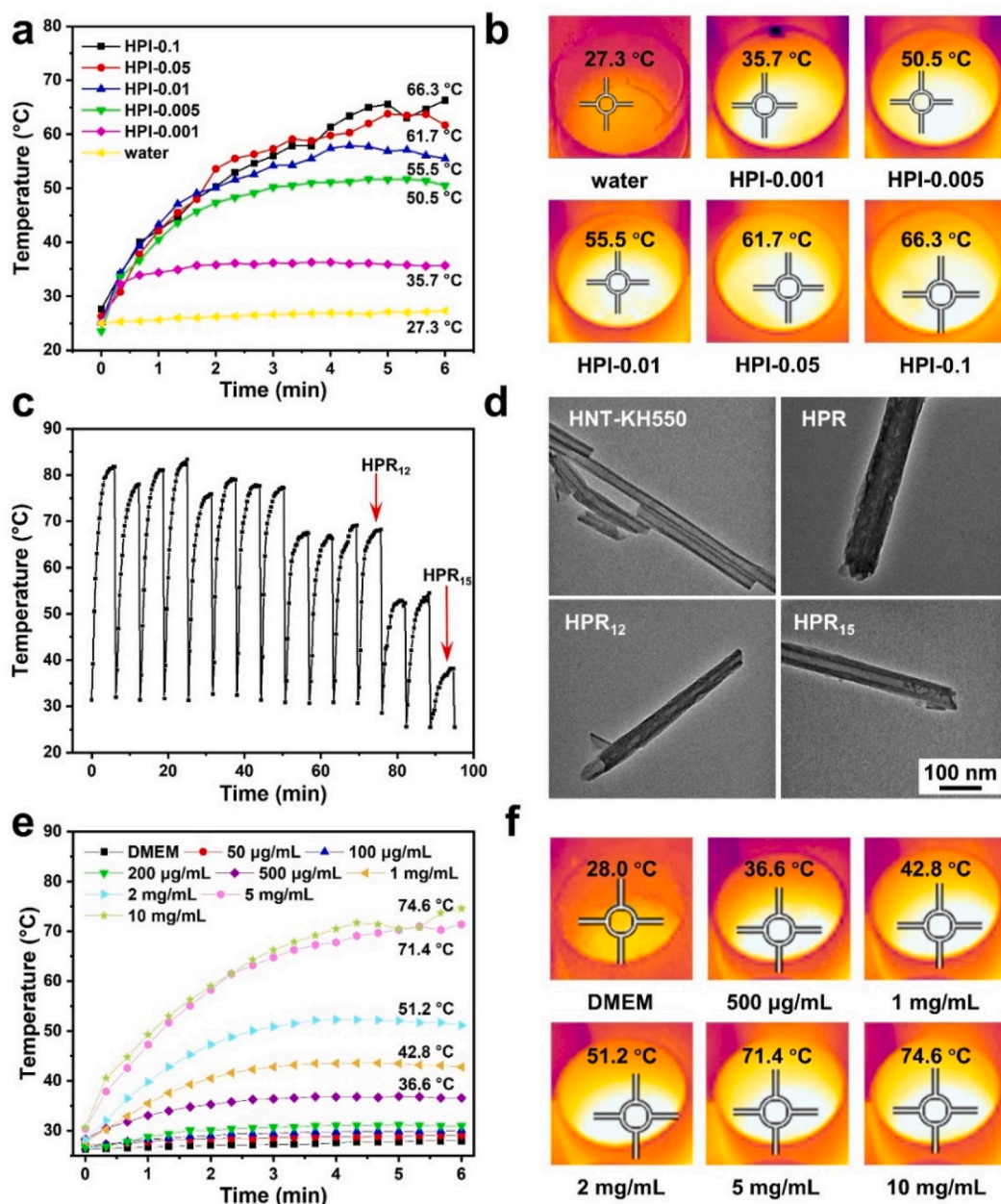


Fig. 2. (a) The temperature raises of nanotubes loaded with ICG and PCM at different ratios upon NIR laser irradiation at 3.0 W/cm<sup>2</sup> for 6 min, and (b) the corresponding infrared thermal images at the end of the irradiation. (c) The photothermal behaviors of HPR suspensions indicated by the temperature changes during 15 cycles of the laser irradiation. (d) The TEM images of HNT-KH550, HPR, HPR<sub>12</sub>, and HPR<sub>15</sub> nanotubes. (e) The temperature raises of HPR suspensions at different concentrations upon 6 min of 3.0 W/cm<sup>2</sup> laser impact, and (f) the corresponding infrared thermal images at the end of the irradiation.

silanization with APTES to improve their dispersion in DMSO (Fig. S1). To make sure the controllability of the system during laser irradiation, we optimized the amount of ICG in the load. As shown in Fig. 2a and b, with the increase of the ICG content, the temperatures of the suspensions of nanotubes were increased, indicating the concentration-related photothermal behaviors. The terminal temperatures of HPI-0.1, HPI-0.05, and HPI-0.01 could reach to above 50 °C within 2 min. For HPI-0.005, upon laser irradiation, the temperature could be raised above 40 °C within 1 min, which was enough for melting PCM, allowing for the subsequent antibacterial drug release from the nanotubes (the terminal temperature was about 50 °C). Therefore, we set the ratio of ICG and PCM as 0.005 to prepare the nanotubes loaded with rifampicin, the antibacterial drug. The mixture of fatty acids, antibiotics, and NIR-absorbing dye were co-loaded into HNTs, and the obtained hybrid halloysite was labeled as HPR. The loading content of rifampicin in the nanotubes was 3.7 µg/mg, and thus the loading efficiency, the mass of drug as a percentage of the total mass of the delivery system, was almost 0.37%. The loading amount of drug in the nanotubes can be regulated by improving the rounds of cyclic air pumping [24] and by increasing the lumen volume in the nanotubes through acid etching [44].

The photothermal stability and cyclic performance of the nanotubes were studied by monitoring the temperature changes of the nanotube suspension upon a NIR laser irradiation for multiple cycles of “on” and “off”. As shown in Fig. 2c, the temperature of the HPR suspension could be elevated up to 50 °C within 6 min. During 12 “on-off” rounds, the temperature changes of the nanotubes showed similar profiles, while the terminal temperatures after about 8 cycles were decreased, which could be attributed to the release of ICG from the nanotubes and the photothermal attenuation of ICG. The temperature still could be increased above the melting point of the PCM. Therefore, the loaded nanotubes HPR showed an efficient photothermal conversion capability along with a good photostability under the laser irradiation up to 15 cycles.

To further demonstrate the encapsulation of the payloads in the nanotubes and their release out from the nanotubes, we observed the morphological change of the nanotubes by TEM. Fig. 2d shows TEM images of the HNT-KH550 nanotubes before and after payload loading, indicating that the hollow cavities of the nanotubes were filled. The diameter of the HPR nanotubes were bigger than that of the other three samples, which was mainly because the outside of the HPR nanotubes could also be coated by the payload. As shown in Fig. 2d, when the HPR suspension was irradiated by the laser for 12 rounds (HPR<sub>12</sub>), less payload was retained inside the nanotubes, and almost all drugs were released from the nanotubes after 15 rounds (HPR<sub>15</sub>). By replacing the drug with rhodamine B, the release process was visualized by fluorescence microscopy method (Fig. S2). These results indicate that the mixed compounds could be loaded into modified HNT nanotubes and then trigger-released due to the melt of PCM upon photothermal heating.

The concentration of HPR suspension could also affect its elevated temperature under the NIR laser irradiation. The photothermal profiles of the loaded nanotubes HPR suspensions at different concentrations are shown in Fig. 2, e–f. The terminal temperatures of the HPR suspensions at a concentration of 10, 5, 2, and 1 mg/mL were 74.6, 71.4, 51.2, and 42.8 °C, respectively, after 6 min laser irradiation at a power density of 3 W/cm<sup>2</sup>. There are sudden changes both in the photothermal curves of HPI-0.1 in Figs. 2a and 10 mg/mL in Fig. 2e at about 5.5 min, which could be attributed to the experimental operation. The highest point of the temperature of the suspensions were monitored by the infrared camera, and the focused position was adjusted during the experiment.

### 3.2. Photothermal triggered release of antibacterial drug from halloysite nanotubes

The cumulative release profiles of rifampicin from the loaded nanotubes HPR suspension (100 mg/mL) in the presence and absence of the laser irradiation were investigated. The temperature of the

suspension was increased after the laser was turned on and quickly reached to the melting point of PCM. As shown in Fig. 3a, rifampicin was released from the nanotubes because of the melting of the gating materials, giving a route out for the drug. In contrast, the release of rifampicin was slow and subtle in the absence of the laser irradiation because solid fatty acids blocked the nanotubes, inhibiting the drug diffusion. By applying the NIR irradiation for several rounds, a pulsed drug release behavior was observed, with its burst release after irradiation followed by minimal release when the laser was switched off, suggesting that the on-demand drug release could be controlled by irradiation. The triggered drug release was retained for 12 rounds (Fig. 3b). The released mass and percentage of rifampicin in the first 6 rounds can be observed from Fig. 3, c–d. The cumulatively released percentage of the drug from the loaded nanotubes HPR was about 32% and 47% after 6 and 12 rounds of laser irradiation, respectively. After 15 rounds of NIR irradiation, the temperature of the HPR suspension could not be raised up to 39 °C, and the 53% rifampicin remaining in the nanotubes could be released further by diffusion to achieve a long-lasting antibacterial ability. In addition, the release profile could also be adjusted by regulating the irradiation parameters. Therefore, one can control and adjust the drug release rate from HNT nanotubes by NIR irradiation. This nanocomposite system can be used for various loads of drug and other biomacromolecules, like proteins and RNA, due to relatively large diameter (ca. 15 nm) of these clay nanotubes.

### 3.3. Characterization of photothermal-responsive composite hydrogels

The digital photos of the pristine alginate hydrogels (ALG), alginate hydrogels containing HP nanotubes (ALG-HP), and alginate hydrogels containing HPR nanotubes (ALG-HPR) are shown in Fig. S3. The photothermal performances of the ALG-HPR composite hydrogels with different concentrations of HPR nanotubes were explored (Fig. 4, a–b). The ALG exhibited a negligible temperature change under the laser irradiation. With the increase of HPR content, the temperature of the ALG-HPR composite hydrogel was increased and reached to 41.9, 47.1, and 48.6 °C for hydrogels containing 20, 25, and 30 wt.% of HPR, respectively. The hydrogel containing 20 wt.% HPR had a terminal temperature of 41.9 °C, which was slightly higher than 39 °C for the co-loaded PCM and allowed only for a moderate release of drug after laser irradiation. When the content of HPR was 30 wt.%, the hydrogel could reach a terminal temperature of 45 °C within 1 min, and such a quick heating rate could result to the poor controllability of the temperature. The hydrogel containing 25 wt.% HPR showed a terminal temperature of 47.1 °C, which was high enough to completely melt PCM, enabling the induced release of the payload from the nanotubes. More importantly, the temperature reached to the equilibrium of 45 °C in 90 s, which was good for preventing skin from scalding. Therefore, we optimized the loading content of nanotubes in alginate hydrogel as 25 wt.% for the following NIR-responsive drug release and wound regeneration. Actually, the temperature raise is related to not only the loading content of the loaded nanotubes in hydrogels but also the power density and the NIR irradiation durations. The content of ICG co-loaded inside the nanotubes was adjusted to suit for the system, and the amount of drug loaded in the composite hydrogel was also related to the HNT content.

The stability of the photothermal performance of ALG-HPR composite hydrogel was further examined. At 39–42 °C while melting of PCM, it is necessary to prevent the skin from scalding; therefore, the laser power was lower to 1.5 W/cm<sup>2</sup> for the first 10 cycles and 2.0 W/cm<sup>2</sup> for the last 13 cycles. As shown in Fig. 4c, during the 23 “on-off” rounds, the hydrogel temperature changes showed similar profiles, while the terminal temperatures after about 18 cycles were decreased, indicating consumption/leakage of ICG, while the melting of inner PCM clogs still occurred. The ALG-HPR composite hydrogel showed an efficient photothermal conversion along with a good photostability under the laser irradiation; however, after 23 cycles the PCM melting was not possible.

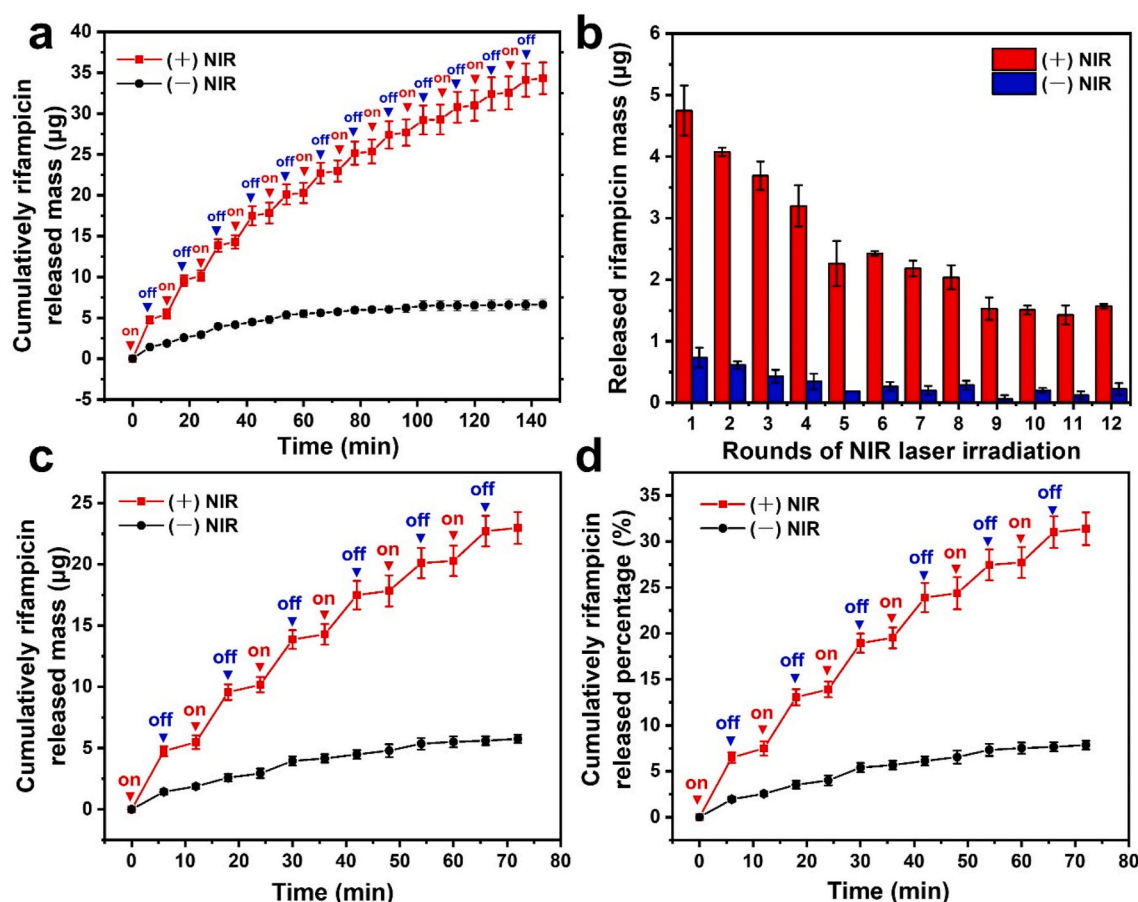


**Fig. 3.** (a) The cumulative release profiles of rifampicin from the suspension of HPR dispersed in DI water at 100 mg/mL upon NIR laser irradiation for multiple cycles of “on” and “off”. (b) Released mass of rifampicin during 12 irradiation rounds. Cumulatively drug released (c) mass and (d) percentage during 6 “on-off” rounds. The red and blue triangles indicate the starting and ending points of irradiation.

The profile of drug released from the ALG-HPR hydrogel was then investigated. Initially, the loading mass of rifampicin in each sample of ALG-HPR hydrogel with a diameter of 15 mm was  $5.1 \pm 1.5 \mu\text{g}$ . From Fig. 4d, the drug was trigger-released during laser irradiation, with only minor release at NIR light interruptions. From Fig. S4a, the triggered release could be retained for 5 rounds, and the cumulatively released percentage of rifampicin was about 90%. As shown in Figure S4b, 5.1 µg/mL of rifampicin could be detected after the 1st round of laser irradiation, which was high enough to inhibit the *S. aureus* proliferation [3]. After 2, 3, 4, and 5 rounds of laser irradiation, the concentrations of cumulatively released drug were 9.1, 15.1, 19.2, and 22.9 µg/mL, respectively. Therefore, upon the laser irradiation, a controlled amount of rifampicin could be released from the hydrogel, which was difficult to be realized by some other drug loading systems based on diffusion or matrix degradation.

### 3.4. In vitro cytotoxicity of the ALG-HRP hydrogel

The biocompatibility of the ALG-HPR hydrogel was investigated by L929 cells. As shown in Fig. 4e, the numbers of L929 cells on the ALG-HPR hydrogel were continuously increased during 8 days of incubation, indicating that the ALG-HPR hydrogel was nontoxic and could support cell proliferation. The cells reached to 70–80% confluence after 4 days and 90% after 8 days incubation, with healthy morphologies (Fig. 4f). Upon the laser irradiation, the loaded components were released from the hydrogel, without affecting L929 cells growth. Moreover, even when the temperature of ALG-HPR hydrogels was up to 42 °C, the growth of L929 cells was not adversely affected. We concluded that the ALG-HPR hydrogels could support the proliferation of L929 cells both in the

absence and presence of irradiation.

### 3.5. Antibacterial activity of composite hydrogels in vitro

To evaluate the antibacterial capability of the composite hydrogel, the laser irradiation conditions were adjusted to avoid the over exposure of bacteria in the air. In this case, the cumulatively released mass and concentration of rifampicin from the ALG-HPR hydrogel under a NIR laser irradiation for multiple cycles of “on” and “off” were detected. As shown in Fig. S5, only a minor concentration of rifampicin was released in the absence of NIR irradiation. After the 1st round of laser irradiation, 1.8 µg/mL of drug was released, which was enough to inhibit the *S. aureus* growth [3]. The concentrations of released rifampicin were increased to 4.9 and 7.4 µg/mL after 2 and 3 rounds of irradiation to enhance the efficacy of bacterial elimination. Fig. S6 shows the photographs of *S. aureus* inhibition zone around the hydrogels after incubation for 24 h at 37 °C. No inhibition zone was observed around ALG and ALG-HP hydrogels, indicating that the whole plate was covered by bacteria. In contrast, distinct inhibition zone was observed around ALG-HPR hydrogels both in the absence and presence of the laser irradiation. The diameter of the inhibition zone was larger in the presence of NIR irradiation.

ALG-HPR hydrogels were also co-cultured with the suspension of *S. aureus* ( $5 \times 10^7$  CFU/mL) to evaluate the effect of the laser driven on-demand release of rifampicin on the bacterial growth. The hydrogels in the absence of laser irradiation served as the control group. The bacterial suspensions were also incubated in the absence or presence of irradiation served as control groups. As shown in Fig. 5a and Fig. S7, the number of bacterial colonies formed in the Blank (+) NIR and Blank (–)

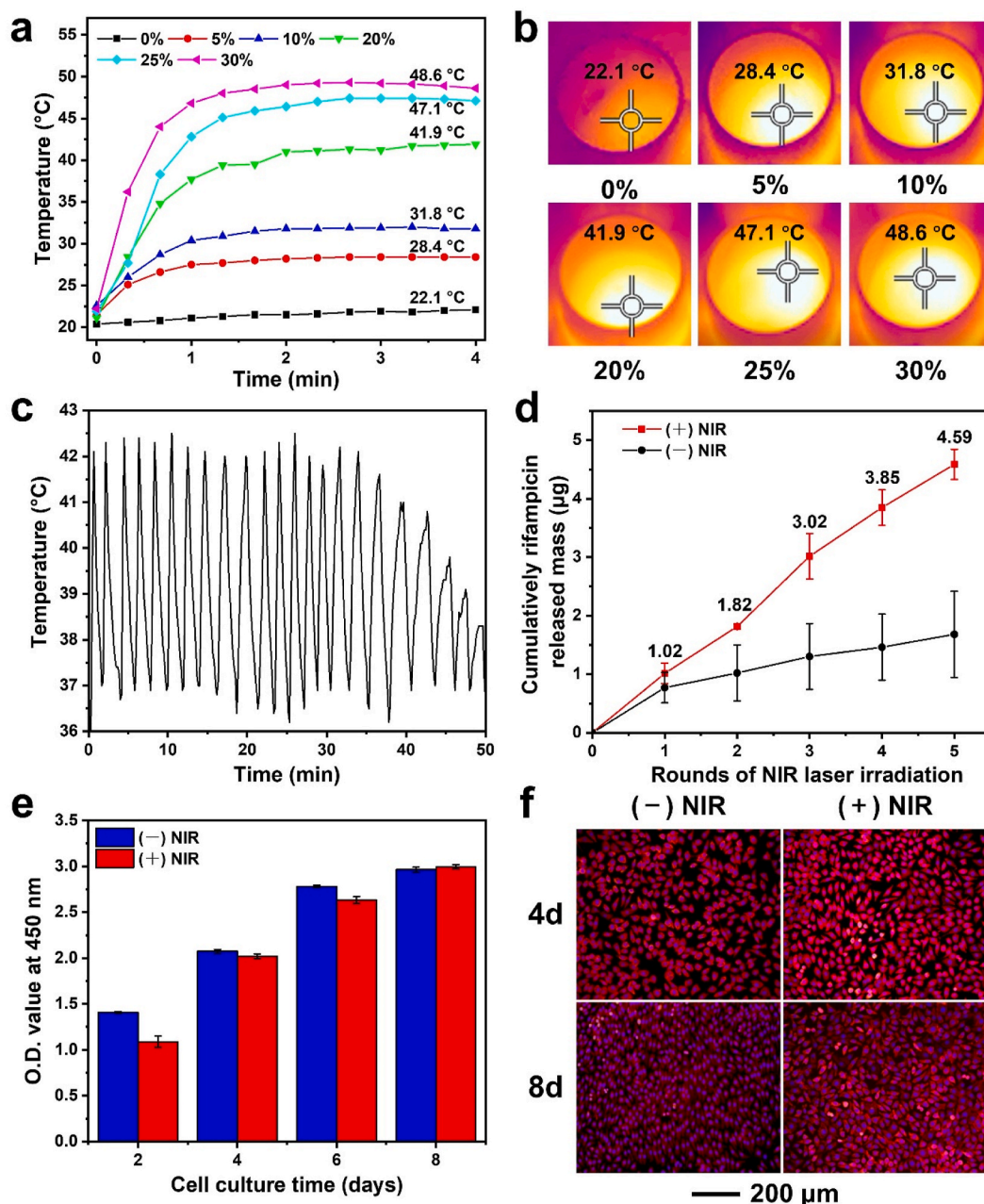


**Fig. 4.** (a) Temperature raises of composite hydrogels containing different concentrations of loaded nanotubes HPR upon laser irradiation at  $3.0 \text{ W/cm}^2$  for 4 min, and (b) the corresponding infrared thermal images. (c) The photothermal behavior of ALG-HPR hydrogel containing 25 wt.% HRP. (d) The cumulative drug release profiles from the ALG-HPR hydrogel containing 25 wt.% HRP in the presence and absence of laser irradiation, respectively. (e) The O.D. values of L929 cells after incubation for 2, 4, 6, and 8 days on the ALG-HPR hydrogel containing 25 wt.% HRP in the presence and absence of laser irradiation, respectively. (f) Fluorescence micrographs of L929 cells cultured on the ALG-HPR hydrogel containing 25 wt.% HRP in the presence and absence of laser irradiation, respectively.

NIR showed no obvious difference, but the number of bacterial colonies decreased with ALG-HPR hydrogels added, no matter in the absence or presence of the laser irradiation. With 3 cycles laser irradiation, the number of bacteria in the ALG-HPR (+) NIR group was significantly decreased, indicating that NIR-triggered release of rifampicin from the ALG-HPR hydrogel could continuously inhibit the growth of *S. aureus*. Without irradiation induced drug release, the survival ratio of bacteria was increased after the initial inhibition of growth, but after laser irradiation, the survival ratio was significantly decreased upon multiple rounds of the laser irradiation, as shown in Fig. 5, b–c. Nearly 100% of *S. aureus* was killed after 3 rounds of laser irradiation, which was attributed to the outstanding photothermally triggered release of the drug from ALG-HPR hydrogel.

The viability of bacteria after incubation with the hydrogel upon laser irradiation was also evaluated and monitored using live/dead staining assay, as shown in Fig. 5d. In the CLSM images, live and dead bacteria were stained with green and red fluorescence via SYTO9/propidium iodide, respectively. Almost no red fluorescence was observed in both Blank (–) NIR and Blank (+) NIR groups, indicating that the growth of *S. aureus* was not adversely affected upon the laser irradiation. The corresponding intensities of green fluorescence of the bacteria in the ALG-HPR groups are shown in Fig. 5, e–f. Without NIR irradiation, there were few green fluorescence spots, but due to the limited content of rifampicin absorbed in the loaded nanotubes HPR, the area of green fluorescence in the image was gradually increased. On the contrary, the areas of green fluorescence in the group of ALG-HPR (+) NIR were kept

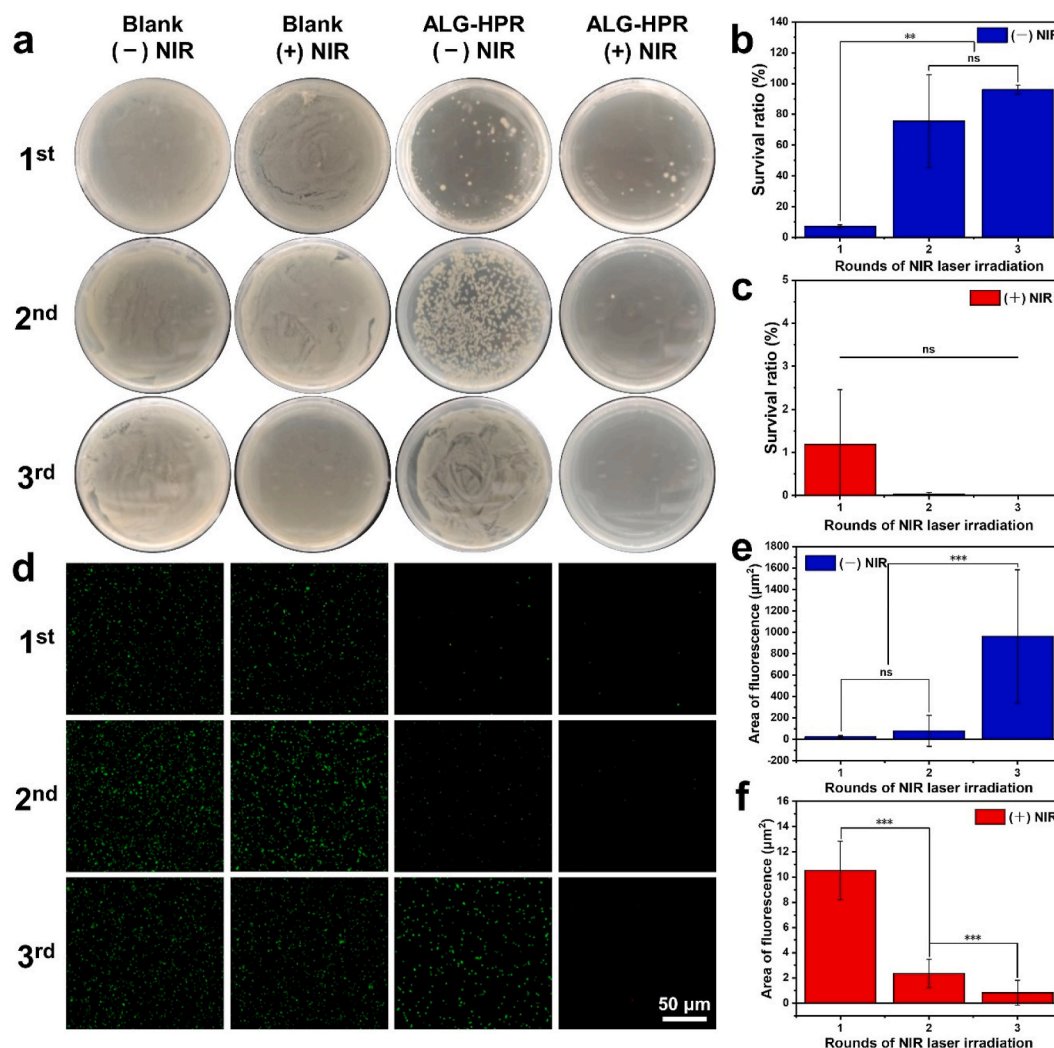


**Fig. 5.** (a) Photographs of the bacterial colonies grown on the culture plates showing antibacterial activities of ALG-25 wt.% HPR hydrogels. The corresponding survival ratio of *S. aureus* cultured with ALG-25 wt.% HPR hydrogels (b) in absence and (c) presence of the laser irradiation. (d) CLSM images of live (green) and dead (red) *S. aureus* cultured on ALG-HPR hydrogels in the absence or presence of the laser irradiation at  $3.0 \text{ W/cm}^2$  for 30 s and repeated 3 times. The corresponding area of green fluorescence for live *S. aureus* cultured with ALG-25 wt.% HPR hydrogels (e) in the absence and (f) presence of the irradiation. The *S. aureus* suspension without hydrogels in the absence or presence of irradiation served as control group (Blank).

at low level and decreased upon multiple rounds of the laser irradiation. After 3 rounds, no green fluorescence was observed, indicating that the drug released from ALG-HPR hydrogels killed majority of *S. aureus*. As quantitated using Image Pro Plus 6.0 software (Fig. 5f), for the ALG-HPR hydrogel exposed to the laser, the intensities of green fluorescence were significantly decreased with the irradiation rounds, indicating that more drug was released from the ALG-HPR hydrogel. An excessive and long-term use of antibiotic treatment can result in the drug resistance of bacteria. Upon the on-demand and multi-step release, the concentration of the antibiotics can be maintained to a certain level to reduce the side effects, which will be beneficial for avoiding drug resistance [3]. Several studies have developed controlled drug release systems to deliver antibiotics in an on-demand and multi-step way to inhibit drug resistance [3, 45].

### 3.6. Wound healing and anti-bacterial efficacy in vivo

A rat infected full-thickness skin wound model allowed for investigation of therapeutic efficacy of ALG-HPR hydrogels against bacteria and promoting wound healing. The rats infected with *S. aureus* were divided into five groups, i.e., *S. aureus* (no treatment), and with addition

of different hydrogel and NIR irradiation: ALG, ALG-HP (+) NIR, ALG-HPR, ALG-HPR (+) NIR. The rats in the Blank group without infection served as the control group. Fig. S8, a–e shows the splint model of full-thickness excision wound on rats and the treatment with hydrogels upon the laser irradiation. Fig. S8f shows the corresponding thermal images of hydrogels on skin wound upon the irradiation. The temperature of the hydrogel maintained at  $39\text{--}42^\circ\text{C}$  during 7 min of laser impact, which was high enough for the melt of co-loaded PCM while preventing the wounds from scalding. Fig. 6a and b, show the photographs of the wounds at day 0, 3, 7, 14, and 21, after different treatments. The ALG-HPR (+) NIR group showed the best performance in the infection inhibiting and promoting the wound healing. In *S. aureus*, ALG, and ALG-HP (+) NIR groups, a certain degree of pyosis appeared at day 3 due to the inoculation of *S. aureus*, which was still observed after 7 days. Meanwhile, the two groups of ALG-HPR and ALG-HPR (+) NIR group involving the use of HPR, no continuous development of pyosis was observed, indicating that the released drug inhibited the bacteria growth. In the presence of the laser irradiation, ALG-HPR (+) NIR group showed a better wound healing, with no pyosis generated.

To quantitatively evaluate the antibacterial activity of ALG-HPR hydrogels upon NIR irradiation, after 7 days, the bacteria maintained

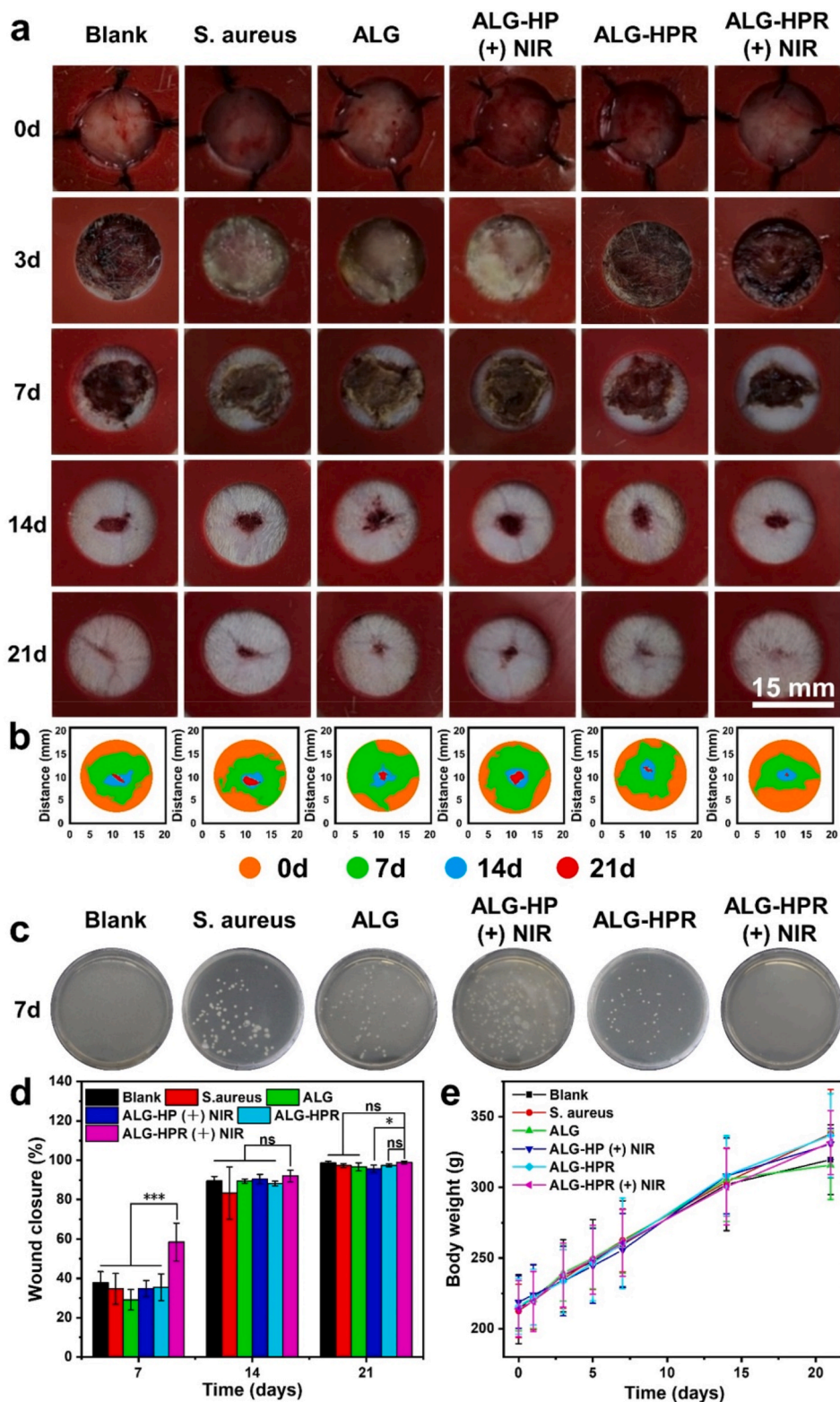


Fig. 6. (a) Photographs of the wounds on the 0, 3, 7, 14, and 21st day after different treatments, and (b) the traces of wound closure. (c) Bacterial colonies grown on 7th day in the culture plate after harvesting from the tissues treated by different groups. (d) The wound closure rates with different methods with time. (e) Body weight changes of the rats during the healing.

around the wound were cultured and counted (Fig. 6c and S9). Upon NIR laser irradiation, there was no bacteria proliferation on the agar plate, whereas bacterial colonies were found in the wound beds of the other treatment groups. Specifically, for the ALG-HPR group in the absence of NIR irradiation, the bacteria could re-grow after the initial

release of rifampicin, while a continuous bacterial inhibition could be realized with pulsing laser initiation of more drug delivered. The percentages of wound closure in the different treatment groups for 21 days were measured, as shown in Fig. 6d. The wounds in all groups were undergoing a healing process, but with different speed. At the early stage

of wound healing within 7 days, the healing effect of ALG-HPR (+) NIR was much more obvious (Fig. 6d). After 21 days, the wound in this group was completely regenerated and covered by new tissue. As shown in Fig. 6e, the body weights of the rats in the different groups were also monitored, with no abnormal behavior.

For *in vivo* toxicity analysis, a biochemical test was conducted to check the numbers of white blood cells, platelets, and red blood cells, and so on, and no adverse effect was detected for used sample treatments (Fig. S10). In conclusion, during multiple rounds of NIR irradiation the ALG-HPR hydrogel could effectively kill the *S. aureus* with a controllable dose of released drug, which is beneficial for preventing drug-resistance bacteria.

### 3.7. Histological analysis during wound regeneration

To further distinguish the qualities of the regenerated skins during wound healing, the hematoxylin and eosin (H&E) staining of wound sections were carried out, as shown in Fig. 7. On day 3, large areas of necrotic cell debris were observed in the wounds of all groups. Except Blank group, there were epithelial erosions in other groups, indicating that the *S. aureus* added at the wound site resulted in the occurrence of infection, and thus the bacterial infection model was successfully established. At the same time, except Blank group, the erosion area of the ALG-HPR (+) NIR group was smaller than that of the other groups. On day 7, the unrepaired wound area was the smallest in ALG-HPR (+)

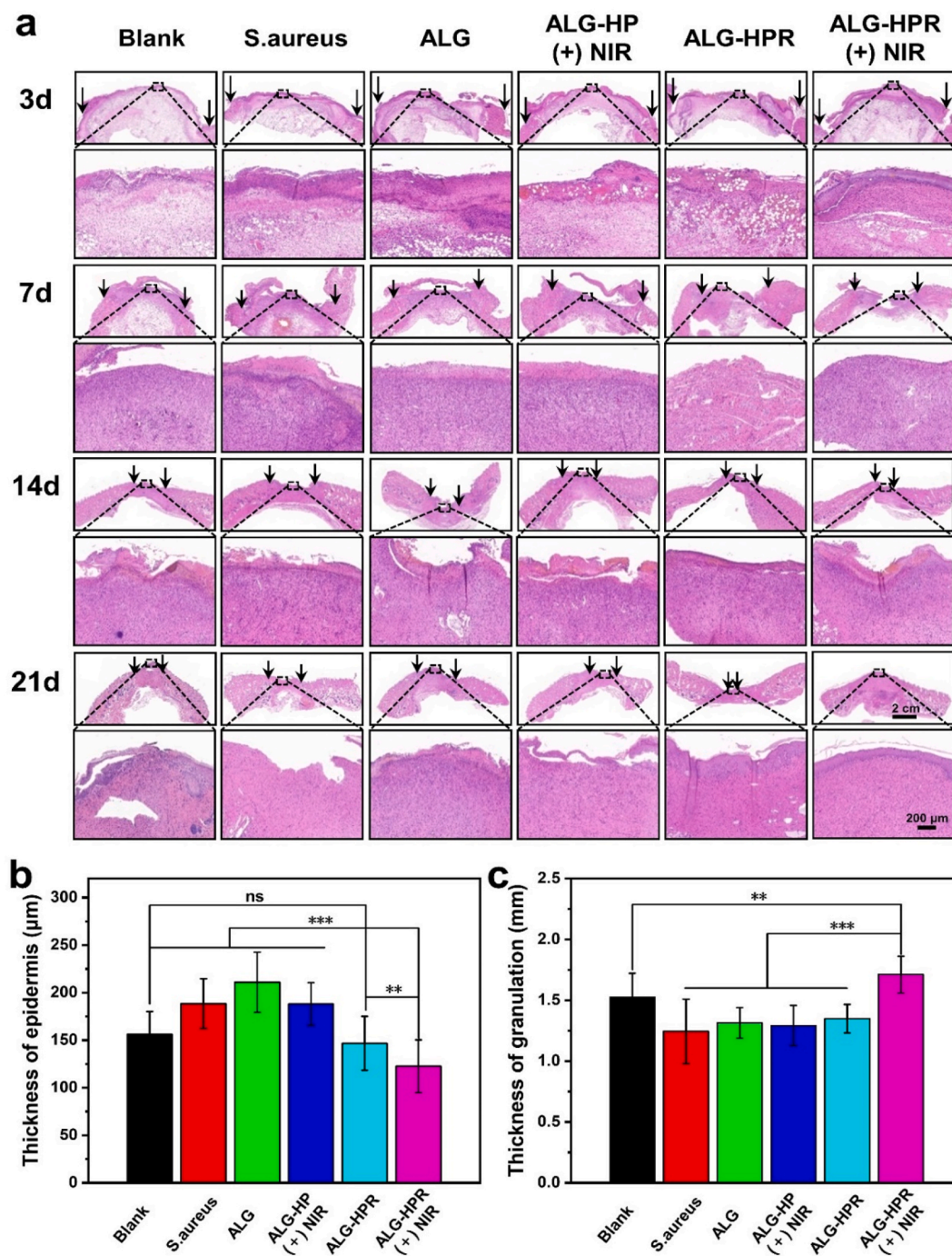


Fig. 7. Accelerated repair and regeneration in *S. aureus*-infected wound. (a) H&E staining images of tissues from different treatment groups on 3, 7, 14, and 21st day. Epidermis and granulation tissue thickness of wounds on 21st day (b–c).

NIR group, and the epithelium had no erosion, while there were still epithelial erosions in *S. aureus*, ALG, ALG-HP (+) NIR, and ALG-HPR groups caused by bacteria infection. After the first week, there was nearly no epidermis structure formed in the Blank control, while regenerated epidermis was observed in the ALG-HPR (+) NIR group. On day 14, the wound healing was in the proliferation stage, and a large area of tissues had been repaired. It was obvious that the unrepaired wound in ALG-HPR (+) NIR group was the narrowest. At the same time, the wound tissues of all groups had new epidermis, and the dermis was replaced by a large area of hyperplasia of connective tissues. The defect regions in the wounds were decreased and the thickness of granulation tissues were increased from day 3 to day 21 in all groups, but induced drug released ALG-HPR (+) NIR group showed the least defect region and the thickest granulation tissue. After 21 days, the surface of the regenerated skin in ALG-HPR (+) NIR group was completely covered by neo-epithelium without scars and showed a complex epidermis structure. As shown in Fig. 7b, the newly formed epidermis was the thinnest in the ALG-HPR (+) NIR group, followed by Blank and ALG-HPR groups. As for the wound caused by bacterial infection, a thicker granulation tissue plays a vital role in wound healing process, acting as an important indicator for evaluating wound repair [46]. The newly formed granulation tissue was also the thickest in the ALG-HPR (+) NIR group followed by Blank group (Fig. 7c). Altogether, the above results suggested that with the treatment of ALG-HPR hydrogel impacted by NIR irradiation, the healing process was essentially accelerated, with neo-epidermis regeneration and abundant granulation tissue formation in the wounds.

### 3.8. Expressions of IL-6 and TNF- $\alpha$ during wound regeneration and angiogenesis

Wound healing undergoes four phases [6], and the second inflammatory phase will be chronic for bacterial infected-wound, which is necessary to inhibit bacterial effectively for wound healing. The immunohistochemistry analysis of both IL-6 and TNF- $\alpha$ , as two pro-inflammatory factors, was performed to examine the anti-infection efficacy of the hydrogels [47–49]. Fig. 8, a–d and Fig. S11 shows the immunohistochemistry staining images and their quantified analysis. The high positive expressions of IL-6 and TNF- $\alpha$  were found in *S. aureus*, ALG, and ALG-HP (+) NIR groups, indicating a serious inflammation response caused by the bacteria. For the ALG-HPR group, a significant decrease of the inflammation response was achieved because of the initial release of rifampicin killing bacteria. Furthermore, in the irradiated ALG-HPR (+) NIR group, both the expressions of IL-6 and TNF- $\alpha$  were the lowest relative to other infected groups, indicating fewer inflammation. This could be attributed to the on-demand drug release killing *S. aureus* proving excellent antibacterial capability of this formulation. The results demonstrated that ALG-HPR hydrogel could resist bacterial infections *in vivo* and reduce the inflammation with controlled laser irradiation, transforming wound from inflammatory to the proliferative phase, which improved the tissue repair rate.

The growth of new capillaries is essential for wound repair, providing nutrition to damaged tissue. CD31 is a *trans*-membrane protein, expressing in early angiogenesis, and it plays an essential role in promoting wound healing [14,50,51]. As shown in Fig. 8, e–f, a higher expression of CD31 was found in the ALG-HPR (+) NIR group, ALG-HPR group, and the Blank group. The positive staining of CD31 was reduced from day 7–21 in all groups, but irradiated ALG-HPR (+) NIR group still

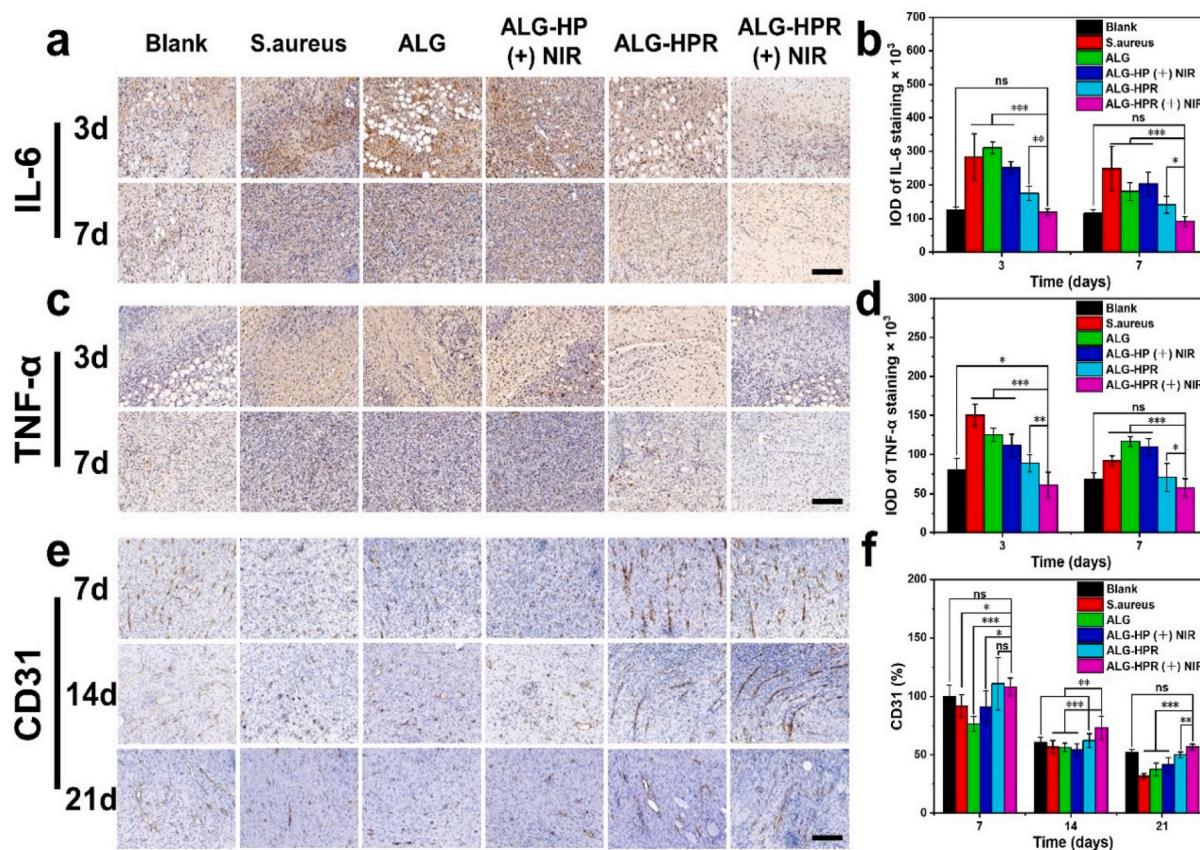


Fig. 8. Immunohistochemistry staining images of (a) IL-6 and (c) TNF- $\alpha$  on 3 and 7th day, scale bars = 200  $\mu$ m. Quantified analysis of percentages of area coverage by (b) IL-6 and (d) TNF- $\alpha$ . (e) The immunohistochemistry staining images of CD31 after 7, 14, and 21 days, respectively. Scale bar = 200  $\mu$ m. (f) Quantified analysis of percentage of area coverage by CD31, the Blank group was set as 100%.

had the highest CD31 expression, demonstrating the best pro-vascularization capability. This could be attributed to the excellent anti-inflammation capability of the ALG-HPR hydrogel in the presence of NIR irradiation, causing more macrophages transforms from pro-inflammatory to anti-inflammatory type and stimulating more endothelial cells, which play vital roles in promoting angiogenesis and initiating the growth of new blood vessels [52].

### 3.9. Collagen deposition in vivo

It is vital for bacterial-infected wound healing to deposit and remodel the proper collagen. Collagen proteins, including type I and III, are the primary constituents in dermal extracellular matrix [53]. Previous studies revealed that early abundant deposition of collagen III would accelerate wound healing and result in scarless skin [53,54]. Masson staining was done to visualize the total collagen proteins [6]. The collagen density and proper type in the regeneration tissues were evaluated by immunohistochemistry staining of collagen I and III, performing on the day 7, 14, and 21 [43]. As shown in Fig. 9, a–b and Fig. S12a, the densities of total collagen proteins were significantly increased from day 7–21 in all groups, and irradiated ALG-HPR (+) NIR group showed the highest collagen density, followed by no irradiation ALG-HPR and Blank groups. On day 21, the wound in ALG-HPR (+) NIR group was completely healed, and skin appendages could be clearly

seen. Fig. 9, c–f and Fig. S12, b–c show the immunohistochemistry staining images and quantitative data of collagen I and III, the two dominant collagen types in the skin. Positive expressions of both collagen I and III increased from day 7 to day 21 in all groups, and irradiated ALG-HPR (+) NIR group showed the highest expression level. Taken together, the ALG-HPR (+) NIR group displayed a significantly higher intensity of collagen deposition when compared to other groups.

### 4. Conclusions

We developed an efficient NIR irradiation-controlled drug release nanoplatform by gating the natural clay nanotubes with PCM and then integrated them in alginate matrix by in situ gelation resulting in NIR-responsive hydrogel (ALG-HPR). Upon the laser irradiation, the photothermal heating generated by NIR-absorbing dye ICG raised temperature above 39 °C, leading to the melt of co-loaded PCM and subsequently triggered on-demand release of the antibacterial drug rifampicin from the hydrogel, while not causing thermal damage to the tissues under the mild heat. ALG-HPR hydrogel showed a good cytocompatibility and antibacterial properties under the NIR laser irradiation. Furthermore, healing of the rat skin wound infected with gangrene *S. aureus* demonstrated that the photothermal-responsive hydrogel inhibited bacterial proliferation and effectively suppressed the inflammatory response caused by *S. aureus* bacteria, thus accelerating wound closure and

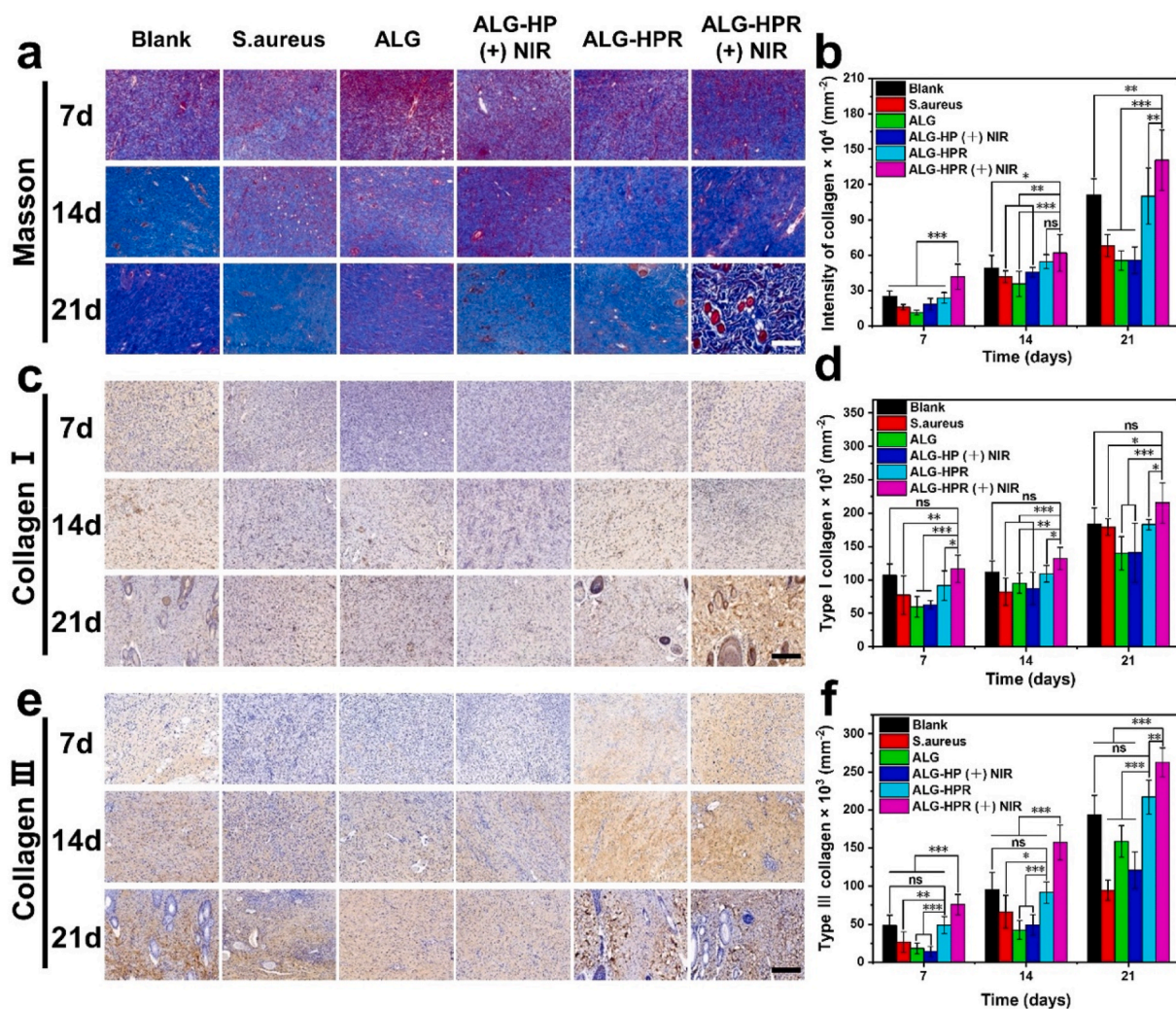


Fig. 9. The collagen deposition and remodeling at wound site in all treatment groups. (a) Masson staining images of tissues on 7, 14, and 21st day, scale bar = 200 μm. (b) Corresponding quantitative data of collagen. Immunohistochemistry staining images of (c) collagen I and (e) collagen III on 7, 14, and 21st day, scale bar = 200 μm, and quantitative data of collagen type (d) I and (f) III.

promoting both angiogenesis and collagen deposition. ALG-HPR hydrogel loaded with drugs has a great potential in the treatment of bacterially infected wounds. Other types of biological effectors, like growth factor proteins could be loaded in the nanotubes and controlled released achieving multiple healing functions. The matrix of the hydrogel can also be regulated to endow the system with more functions. For example, in some cases, the long-term release of drug is also important, especially for inhibiting the prolonged bacterial proliferation. The degree of swelling and degradation time of the hydrogel matrix will play an important role in the drug release profile. To achieve the on-demand release of drug in a long-term profile, we can regulate the degree of swelling and degradation time of the hydrogel matrix by modifying the components, composition, and the cross-linking degree of the hydrogel. In addition, the hydrogel can also be mixed with cells to further promote the wound healing and tissue regeneration. This work offers a facile strategy for the construction of biocompatible, NIR-responsive step-wise drug release platforms for tissue engineering and medicine.

### Ethics approval and consent to participate

During the entire experiment, the rats were treated in accordance with the guidelines for Care and Use of Laboratory Animals of Beijing HFK BioScience Co., Ltd Animal Ethics Committee (IACUC-20201225).

### CRediT authorship contribution statement

**Jing-Jing Ye:** Conceptualization, Methodology, Investigation, Writing – original draft. **Long-Fei Li:** Investigation, Writing – original draft. **Rui-Nan Hao:** Investigation, Writing – original draft. **Min Gong:** Writing – original draft. **Tong Wang:** Investigation. **Jian Song:** Investigation. **Qing-Han Meng:** Conceptualization, Methodology. **Na-Na Zhao:** Conceptualization, Methodology. **Fu-Jian Xu:** Conceptualization, Methodology. **Yuri Lvov:** Conceptualization, Writing – original draft, finalizing of the study. **Li-Qun Zhang:** Conceptualization, Methodology, Writing – original draft, finalizing of the study. **Jia-Jia Xue:** Conceptualization, Supervision, Methodology, Writing – original draft, finalizing of the study.

### Declaration of competing interest

The authors declare that they have no competing interests.

### Acknowledgements

This research was funded by the National Natural Science Foundation of China (Grant No. 82002049 and 52073014; to J. X.), Key Program of Beijing Natural Science Foundation (Z200025), and Fundamental Research Funds for the Central Universities (buctrc202020). YL thanks support by T. Pipes Nano Microsystem Endowment, Louisiana Tech University, USA.

### Appendix A. Supplementary data

Supplementary data to this article can be found online at <https://doi.org/10.1016/j.bioactmat.2022.08.026>.

### References

- [1] L. Zhou, H. Zheng, Z. Liu, S. Wang, Z. Liu, F. Chen, H. Zhang, J. Kong, F. Zhou, Q. Zhang, Conductive antibacterial hemostatic multifunctional scaffolds based on Ti<sub>3</sub>C<sub>2</sub>Tx MXene nanosheets for promoting multidrug-resistant bacteria-infected wound healing, *ACS Nano* 15 (2) (2021) 2468–2480.
- [2] G. Han, R. Ceilley, Chronic wound healing: a review of current management and treatments, *Adv. Ther.* 34 (2017) 599.
- [3] Y. Wu, Z. Song, H. Wang, H. Han, Endogenous stimulus-powered antibiotic release from nanoreactors for a combination therapy of bacterial infections, *Nat. Commun.* 10 (1) (2019) 4464.
- [4] A. Wang, S. Duan, X. Ding, N. Zhao, Y. Hu, X. Ding, F.J. Xu, Bioswitchable antibacterial coatings enable self-sterilization of implantable healthcare dressings, *Adv. Funct. Mater.* 31 (18) (2021), 2011165.
- [5] Y. Dhar, Y. Han, Current developments in biofilm treatments: wound and implant infections, *Eng. Regen.* 1 (2020) 64–75.
- [6] Z. Wang, W. Hu, W. You, G. Huang, W. Tian, C. Huselstein, C.-L. Wu, Y. Xiao, Y. Chen, X. Wang, Antibacterial and angiogenic wound dressings for chronic persistent skin injury, *Chem. Eng. J.* 404 (2021), 126525.
- [7] W. Weng, J. Chi, X. Wang, K. Shi, F. Ye, Y. Zhao, Ellipsoidal porous patch with anisotropic cell inducing ability for inhibiting skin scar formation, *Eng. Regen.* 3 (2022) 262–269.
- [8] S. Yao, Y. Luo, Y. Wang, Engineered microneedles arrays for wound healing, *Eng. Regen.* 3 (2022) 232–240.
- [9] H.P. Lee, A.K. Gaharwar, Light-responsive inorganic biomaterials for biomedical applications, *Adv. Sci.* 7 (17) (2020), 2000863.
- [10] Y. Liu, Y. Xiao, Y. Cao, Z. Guo, F. Li, L. Wang, Construction of chitosan-based hydrogel incorporated with antimone nanosheets for rapid capture and elimination of bacteria, *Adv. Funct. Mater.* 30 (35) (2020), 2003196.
- [11] J. Li, Y.J. Wang, J.H. Yang, W.G. Liu, Bacteria activated-macrophage membrane-coated tough nanocomposite hydrogel with targeted photothermal antibacterial ability for infected wound healing, *Chem. Eng. J.* 420 (2021), 127638.
- [12] H.F. Zhang, S.Y. Zheng, C.W. Chen, D.G. Zhang, A graphene hybrid supramolecular hydrogel with high stretchability, self-healable and photothermally responsive properties for wound healing, *RSC Adv.* 11 (11) (2021) 6367–6373.
- [13] M. Li, Y. Liang, Y. Liang, G. Pan, B. Guo, Injectable stretchable self-healing dual dynamic network hydrogel as adhesive anti-oxidant wound dressing for photothermal clearance of bacteria and promoting wound healing of MRSA infected motion wounds, *Chem. Eng. J.* 427 (2022), 132039.
- [14] X. Zhao, Y. Liang, Y. Huang, J. He, Y. Han, B. Guo, Physical double-network hydrogel adhesives with rapid shape adaptability, fast self-healing, antioxidant and NIR/pH stimulus-responsiveness for multidrug-resistant bacterial infection and removable wound dressing, *Adv. Funct. Mater.* 30 (17) (2020), 1910748.
- [15] J. He, M. Shi, Y. Liang, B. Guo, Conductive adhesive self-healing nanocomposite hydrogel wound dressing for photothermal therapy of infected full-thickness skin wounds, *Chem. Eng. J.* 394 (2020), 124888.
- [16] L. Zhou, W. Pi, S. Cheng, Z. Gu, K. Zhang, T. Min, W. Zhang, H. Du, P. Zhang, Y. Wen, Multifunctional DNA hydrogels with hydrocolloid-cotton structure for regeneration of diabetic infectious wounds, *Adv. Funct. Mater.* 31 (48) (2021), 2106167.
- [17] C. Cao, N. Yang, Y. Zhao, D. Yang, Y. Hu, D. Yang, X. Song, W. Wang, X. Dong, Biodegradable hydrogel with thermo-response and hemostatic effect for photothermal enhanced anti-infective therapy, *Nano Today* 39 (2021), 101165.
- [18] C. Zhu, D. Huo, Q. Chen, J. Xue, S. Shen, Y. Xia, A eutectic mixture of natural fatty acids can serve as the gating material for near-infrared-triggered drug release, *Adv. Mater.* 29 (2017), 1703702.
- [19] R. Chen, C. Zhao, Z. Chen, X. Shi, H. Zhu, Q. Bu, L. Wang, C. Wang, H. He, A bionic cellulose nanofiber-based nanocage wound dressing for NIR-triggered multiple synergistic therapy of tumors and infected wounds, *Biomaterials* 281 (2022), 121330.
- [20] W.N. Wang, C.Y. Zhang, M.F. Zhang, P. Pei, W. Zhou, Z.B. Zha, M. Shao, H.S. Qian, Precisely photothermal controlled releasing of antibacterial agent from Bi<sub>2</sub>S<sub>3</sub> hollow microspheres triggered by NIR light for water sterilization, *Chem. Eng. J.* 381 (2020), 122630.
- [21] Y. Xu, C. Zhao, X. Zhang, J. Xu, L. Yang, Z. Zhang, Z. Gao, Y.Y. Song, Engineering tailorable TiO<sub>2</sub> nanotubes for NIR-controlled drug delivery, *Nano Res.* 14 (11) (2021) 4046–4055.
- [22] W.-L. Chiang, T.-T. Lin, R. Sureshbabu, W.-T. Chia, H.-C. Hsiao, H.-Y. Liu, C.-M. Yang, H.-W. Sung, A rapid drug release system with a NIR light-activated molecular switch for dual-modality photothermal/antibiotic treatments of subcutaneous abscesses, *J. Contr. Release* 199 (2015) 53–62.
- [23] G. Gao, Y.W. Jiang, H.R. Jia, F.G. Wu, Near-infrared light-controllable on-demand antibiotics release using thermo-sensitive hydrogel-based drug reservoir for combating bacterial infection, *Biomaterials* 188 (2019) 83–95.
- [24] Y. Lvov, W. Wang, L. Zhang, R. Fakhruddin, Halloysite clay nanotubes for loading and sustained release of functional compounds, *Adv. Mater.* 28 (6) (2016) 1227–1250.
- [25] J. Xue, Y. Niu, M. Gong, R. Shi, D. Chen, L. Zhang, Y. Lvov, Electrospun microfiber membranes embedded with drug-loaded clay nanotubes for sustained antimicrobial protection, *ACS Nano* 9 (2) (2015) 1600–1612.
- [26] J. Xue, C. Zhu, J. Li, H. Li, Y. Xia, Integration of phase-change materials with electrospun fibers for promoting neurite outgrowth under controlled release, *Adv. Funct. Mater.* 28 (15) (2018), 1705563.
- [27] J. Qiu, D. Huo, J. Xue, G. Zhu, H. Liu, Y. Xia, Encapsulation of a phase-change material in nanocapsules with a well-defined hole in the wall for the controlled release of drugs, *Angew. Chem., Int. Ed. Engl.* 58 (31) (2019) 10606–10611.
- [28] H. Cheng, D. Huo, C. Zhu, S. Shen, W. Wang, H. Li, Z. Zhu, Y. Xia, Combination cancer treatment through photothermally controlled release of selenous acid from gold nanocages, *Biomaterials* 178 (2018) 517–526.
- [29] S. Shen, C. Zhu, D. Huo, M. Yang, J. Xue, Y. Xia, A hybrid nanomaterial for the controlled generation of free radicals and oxidative destruction of hypoxic cancer cells, *Angew. Chem., Int. Ed. Engl.* 56 (30) (2017) 8801–8804.
- [30] J. Qiu, D. Huo, Y. Xia, Phase-change materials for controlled release and related applications, *Adv. Mater.* 32 (25) (2020), 2000660.
- [31] W.C. Huang, R. Ying, W. Wang, Y. Guo, Y. He, X. Mo, C. Xue, X. Mao, A macroporous hydrogel dressing with enhanced antibacterial and anti-

- inflammatory capabilities for accelerated wound healing, *Adv. Funct. Mater.* 30 (21) (2020), 2000644.
- [32] J. Ren, X. Yin, Y. Chen, Y. Chen, H. Su, K. Wang, L. Zhang, J. Zhu, C. Zhang, Alginate hydrogel-coated syringe needles for rapid haemostasis of vessel and viscera puncture, *Biomaterials* 249 (2020), 120019.
- [33] T. Cui, X. Li, S. He, D. Xu, L. Yin, X. Huang, S. Deng, W. Yue, W. Zhong, Instant self-assembly peptide hydrogel encapsulation with fibrous alginate by microfluidics for infected wound healing, *ACS Biomater. Sci. Eng.* 6 (9) (2020) 5001–5011.
- [34] X. He, Y. Ding, W. Xie, R. Sun, N.C. Hunt, J. Song, X. Sun, C. Peng, Q. Zeng, Y. Tan, Y. Liu, Rubidium-containing calcium alginate hydrogel for antibacterial and diabetic skin wound healing applications, *ACS Biomater. Sci. Eng.* 5 (9) (2019) 4726–4738.
- [35] J. Zhou, W. Liu, X. Zhao, Y. Xian, W. Wu, X. Zhang, N. Zhao, F.-J. Xu, C. Wang, Natural melanin/alginate hydrogels achieve cardiac repair through ROS scavenging and macrophage polarization, *Adv. Sci.* 8 (20) (2021), 2100505.
- [36] D.R. Sahoo, T. Biswal, Alginate and its application to tissue engineering, *SN Appl. Sci.* 3 (1) (2021) 30.
- [37] P. Ghaderinejad, N. Najmuddin, Z. Bagher, M. Saeed, S. Karimi, S. Simorgh, M. Pezeshki-Modaress, An injectable anisotropic alginate hydrogel containing oriented fibers for nerve tissue engineering, *Chem. Eng. J.* 420 (2021), 130465.
- [38] J.Y. Sun, X. Zhao, W.R. Illeperuma, O. Chaudhuri, K.H. Oh, D.J. Mooney, J. J. Vlassak, Z. Suo, Highly stretchable and tough hydrogels, *Nature* 489 (7414) (2012) 133–136.
- [39] H. Zhao, X. Lv, J. Huang, S. Huang, H. Zhou, H. Wang, Y. Xu, J. Wang, J. Wang, Z. Liu, Two-phase releasing immune-stimulating composite orchestrates protection against microbial infections, *Biomaterials* 277 (2021), 121106.
- [40] W. Yu, Y.-Y. Jiang, T.-W. Sun, C. Qi, H. Zhao, F. Chen, Z. Shi, Y.-J. Zhu, D. Chen, Y. He, Design of a novel wound dressing consisting of alginate hydrogel and simvastatin-incorporated mesoporous hydroxyapatite microspheres for cutaneous wound healing, *RSC Adv.* 6 (106) (2016) 104375–104387.
- [41] S. Shafei, M. Khanmohammadi, R. Heidari, H. Ghanbari, V. Taghdiri Nooshabadi, S. Farzamfar, M. Akbariqomi, N.S. Sanikhani, M. Absalan, G. Tavoosidana, Exosome loaded alginate hydrogel promotes tissue regeneration in full-thickness skin wounds: an in vivo study, *J. Biomed. Mater. Res.* 108 (3) (2020) 545–556.
- [42] L. Sheng, Z. Zhang, Y. Zhang, E. Wang, B. Ma, Q. Xu, L. Ma, M. Zhang, G. Pei, J. Chang, A novel "hot spring"-mimetic hydrogel with excellent angiogenic properties for chronic wound healing, *Biomaterials* 264 (2021), 120414.
- [43] Z. Tu, M. Chen, M. Wang, Z. Shao, X. Jiang, K. Wang, Z. Yao, S. Yang, X. Zhang, W. Gao, C. Lin, B. Lei, C. Mao, Engineering bioactive M2 macrophage-polarized anti-inflammatory, antioxidant, and antibacterial scaffolds for rapid angiogenesis and diabetic wound repair, *Adv. Funct. Mater.* 31 (30) (2021), 2100924.
- [44] A.C. Santos, C. Ferreira, F. Veiga, A.J. Ribeiro, A. Panchal, Y. Lvov, A. Agarwal, Halloysite clay nanotubes for life sciences applications: from drug encapsulation to bioscaffold, *Adv. Colloid Interface Sci.* 257 (2018) 58–70.
- [45] G. Qing, X. Zhao, N. Gong, J. Chen, X. Li, Y. Gan, Y. Wang, Z. Zhang, Y. Zhang, W. Guo, Y. Luo, X. Liang, Thermo-responsive triple-function nanotransporter for efficient chemo-photothermal therapy of multidrug-resistant bacterial infection, *Nat. Commun.* 10 (2019) 4336.
- [46] Y. Liang, X. Zhao, T. Hu, B. Chen, Z. Yin, P.X. Ma, B. Guo, Adhesive hemostatic conducting injectable composite hydrogels with sustained drug release and photothermal antibacterial activity to promote full-thickness skin regeneration during wound healing, *Small* 15 (12) (2019), 1900046.
- [47] G. Chen, Y. Yu, X. Wu, G. Wang, J. Ren, Y. Zhao, Bioinspired multifunctional hybrid hydrogel promotes wound healing, *Adv. Funct. Mater.* 28 (33) (2018), 1801386.
- [48] L. Wang, K. Yang, X. Li, X. Zhang, D. Zhang, L.N. Wang, C.S. Lee, A double-crosslinked self-healing antibacterial hydrogel with enhanced mechanical performance for wound treatment, *Acta Biomater.* 124 (2021) 139–152.
- [49] W. Liu, W. Ou-Yang, C. Zhang, Q. Wang, X. Pan, P. Huang, C. Zhang, Y. Li, D. Kong, W. Wang, Synthetic polymeric antibacterial hydrogel for methicillin-resistant staphylococcus aureus-infected wound healing: nanoantimicrobial self-assembly, drug- and cytokine-free strategy, *ACS Nano* 14 (10) (2020) 12905–12917.
- [50] M. Li, Y.P. Liang, J.H. He, H.L. Zhang, B.L. Guo, Two-pronged strategy of biomechanically active and biochemically multifunctional hydrogel wound dressing to accelerate wound closure and wound healing, *Chem. Mater.* 32 (23) (2020) 9937–9953.
- [51] W. Zhao, Y. Li, X. Zhang, R. Zhang, Y. Hu, C. Boyer, F.J. Xu, Photo-responsive supramolecular hyaluronic acid hydrogels for accelerated wound healing, *J. Contr. Release* 323 (2020) 24–35.
- [52] H. Ramphul, F. Gimie, J. Andries, D. Jhurry, A. Bhaw-Luximon, Sugar-cane bagasse cellulose-based scaffolds promote multi-cellular interactions, angiogenesis and reduce inflammation for skin tissue regeneration, *Int. J. Biol. Macromol.* 157 (2020) 296–310.
- [53] C. Wang, M. Wang, T. Xu, X. Zhang, C. Lin, W. Gao, H. Xu, B. Lei, C. Mao, Engineering bioactive self-healing antibacterial exosomes hydrogel for promoting chronic diabetic wound healing and complete skin regeneration, *Theranostics* 9 (1) (2019) 65–76.
- [54] S. He, T. Walimbe, H. Chen, K. Gao, P. Kumar, Y. Wei, D. Hao, R. Liu, D.L. Farmer, K.S. Lam, J. Zhou, A. Panitch, A. Wang, Bioactive extracellular matrix scaffolds engineered with proangiogenic proteoglycan mimetics and loaded with endothelial progenitor cells promote neovascularization and diabetic wound healing, *Bioact. Mater.* 10 (2022) 460–473.